Applied Catalysis B: Environmental 301 (2022) 120830

Contents lists available at ScienceDirect

Applied Catalysis B: Environmental

journal homepage: www.elsevier.com/locate/apcatb

Highly active atomically dispersed platinum-based electrocatalyst for hydrogen evolution reaction achieved by defect anchoring strategy

Yawen Chen, Rui Ding, Jia Li *, Jianguo Liu *

National Laboratory of Solid State Microstructures, College of Engineering and Applied Sciences, and Collaborative Innovation Center of Advanced Microstructures, Nanjing University, 22 Hankou Road, Nanjing 210093, China

ARTICLE INFO

Keywords:
Water splitting
Hydrogen evolution
Single-atom catalyst
Platinum
Defects
Electrocatalyst

ABSTRACT

Single-atom catalysts (SACs) can achieve ultimate atomic utilization of precious metals to improve water splitting's economy. However, active sites in SACs are usually insufficient. Therefore, we propose the use of porous Co_1NC which is rich in defects as support to prepare Pt_1/Co_1NC by mild electrochemical reduction at room temperature. Pt_1/Co_1NC showed record-high hydrogen evolution reaction (HER) activity, with an overpotential of only 4.15 mV at a current density of 10 mA cm^{-2}. Its mass activity reached 32.4 A mg^{-1}Pt at an overpotential of 20 mV, which is 54 times that of Pt/C. The turnover frequency was up to 32.86 s^{-1} at 20 mV, with excellent stability in long-term service. Our strategy suggests that nitrogen/carbon defects are vital for anchoring&forming monodispersed Pt active sites while preventing agglomeration. These sites possess low energy barriers, as verified by theoretical simulations. Therefore, our method presents a technical breakthrough for reducing cost of hydrogen energy.

1. Introduction

Hydrogen energy has attracted wide attention, as it is regarded as the most promising candidate for the next generation of environmentally friendly energy [1–4]. One promising way to achieve true zero carbon emission with hydrogen energy is to use clean electricity generated by wind and solar power to split water [5,6]. However, the hydrogen evolution reaction (HER) that takes place in the cathode relies heavily on precious metal catalysts, which hinders its popularization [7–10]. Recently, the rapid development of single atomic catalysts (SACs) has led to significant breakthroughs [11–14]. In SACs, every single transition metal atom can be exploited as an active site, and atomic utilization can reach up to one hundred percent. This enables SACs to achieve excellent catalytic activity at very low precious-metal loads. Moreover, the unique effect brought by electronic metal–support interaction could further lead to high intrinsic catalytic activity [15]. However, the majority of reported SACs that serve as electrocatalysts are carbon-based. Moreover, they need to undergo high-temperature calcination, which consumes a great amount of energy, and complex procedures are required for the precursor and post-treatment [16,17]. Moreover, the abundance of active sites in SACs is insufficient because high metal loading leads to the agglomeration of metal species. Therefore, the support of SACs needs to have strong interactions with the metal atoms. Recently, numerous studies have shown that defects can offer a satisfactory solution [18–21]. For example, Zhang et al. reported that the synergistic effect of atomic Pt-Co located on a defected C/N graphene surface in A-CoPt-NC can lead to ultrahigh oxygen reduction reaction (ORR) activity [22]. Qu et al. captured $Cu(NH_3)_x$ species with defects on a nitrogen-rich carbon support to form isolated copper sites in an ammonia atmosphere [23]. Widespread defects in carbon materials have been found not only to possess intrinsic catalytic activities, but also to provide anchoring sites for trapping metal atoms to prevent agglomeration [24,25]. Therefore, the design of a support rich in defects is helpful for increasing the density of catalytic sites. In this study, Co-doped zeolite imidazole framework-8 (ZIF-8)-derived porous carbon, with abundant defects, was used to adsorb Pt precursors. After a mild electrochemical reduction at room temperature, Pt_1/Co_1NC with atomically dispersed Pt and Co was obtained. The catalyst containing two types of single atoms showed an extremely low overpotential of 4.15 mV at a current density of 10 mA cm^{-2} for HER in 0.5 M H_2SO_4. Its mass activity reached 32.4 A mg^{-1}_{Pt} at an overpotential of 20 mV and showed excellent stability. This effective strategy can be extended to catalysts containing other porous supports and precious metals.

* Corresponding authors.
E-mail addresses: lijia0226@nju.edu.cn (J. Li), jianguoliu@nju.edu.cn (J. Liu).

https://doi.org/10.1016/j.apcatb.2021.120830
Received 17 August 2021; Received in revised form 22 September 2021; Accepted 13 October 2021
Available online 16 October 2021

2. Experimental section

2.1. Synthesis of Co_1NC

A total of 1435.5 mg of 2-methylimidazole was dissolved in 180 mL of methanol and mixed uniformly by ultrasound to obtain solution A. A total of 1250.5 mg of zinc nitrate hexahydrate and 22.5 mg of cobalt (II) nitrate hexahydrate was dissolved in 180 mL of methanol and mixed uniformly by ultrasound to obtain solution B. Solution A and solution B were mixed with ultrasound for 3 min to obtain solution C. Then, 360 mL of solution C was evenly poured into 12 hydrothermal kettle linings. The volume of the hydrothermal synthesis reactor was 50 mL. After assembly of the hydrothermal synthesis reactor, it was placed in an oven at 120 °C for 6 h. The precipitate in the hydrothermal synthesis reactor was collected and washed three times with methanol centrifugation at 12,000 rpm for 5 min. After centrifugation, the samples were placed in an oven to dry at 60 °C for 12 h. After drying, Co-ZIF was obtained by grinding the samples with a mortar for 20 min. Co-ZIF powder was placed in a porcelain boat and heat-treated at 1100 °C for 3 h in a tubular furnace at a heating rate of 5°/min. After the heat treatment was completed, Co_1NC was obtained.

2.2. Synthesis of NC

The preparation method is similar to that for Co_1NC; the difference is that no cobalt (II) nitrate hexahydrate was added to the raw material.

2.3. Synthesis of Pt_1/Co_1NC

A total of 50 mL of ultrapure water was poured into a 100-mL beaker, and 119.4 μl of an aqueous solution of chloroplatinic acid (concentration 3.77 $mg_{Pt}\,mL^{-1}$) was added to the water, which was magnetically stirred for 30 min. Then, 50 mg of Co_1NC was added to the above solution, which was stirred at 25 °C for 8 h. A vacuum filter device was used to filter the above solution, and ultrapure water was used for filtering. After filtration, the filter membrane was removed and placed in a beaker. After sealing with the sealing membrane, several small holes were cut, and the beaker was placed in a vacuum oven to dry at 60 °C for 8 h to obtain $[PtCl_6]^{2-}/Co_1NC$. Next, 30 mg of $[PtCl_6]^{2-}/Co_1NC$ was added to a glass bottle, to which was then added 250 μl of ultrapure water, 21,600 μl of ethanol, and 90 μl of Nafion (5 wt%); this solution was treated with ultrasound for 20 min to ensure that the mixture was evenly mixed. Then, 200 μl of the ink was absorbed with a pipette and evenly coated on a 2 cm × 2 cm glassy carbon sheet. An infrared lamp and a small fan were used to accelerate the drying rate. The glassy carbon sheet was clamped with a platinum electrode and placed in an N_2-saturated 0.1 M perchloric acid solution. A graphite rod and an electrolyzed standard hydrogen electrode were also placed into the perchloric acid solution to form a three-electrode system, in which the platinum electrode was the working electrode, the graphite rod was the counter electrode, and the standard hydrogen electrode was the reference electrode.

Using a CHI760, cyclic scanning voltammetry was selected with a scanning potential range of 1–1.2 V vs. RHE at a scanning speed of 20 mV s^{-1}, and scanning was conducted until the CV curve no longer changed. This reduction process was repeated several times. The catalyst on the glassy carbon sheet was supersonicated into ethanol, after which the ethanol was filtered out so that the catalyst was stuck to the filter membrane. The filter membrane was placed in a beaker and dried under vacuum at 60 °C for 8 h. The dried powder was ground to obtain Pt_1/Co_1NC. Samples with different Pt loads were prepared by changing the amount of chloroplatinic acid added.

2.4. Synthesis of Pt_{NP}/NC

The preparation method is similar to that of Pt_1/Co_1NC; the difference is that NC was used as a carrier.

2.5. Electrochemical measurements

The HER catalytic performance was tested using a CHI760e. First, the ink was prepared, and 6 mg of Pt_1/Co_1NC, 50 μl of ultrapure water, 432 μl of ethanol, and 18 μl of Nafion (5 wt%) were ultrasonically mixed to evenly disperse the slurry. Then, a pipette was used to absorb 10 μl of ink droplets on a rotating disk electrode (RDE, glassy carbon electrode diameter: 5 mm, area: 0.19625 cm^2), which was dried at room temperature. A three-electrode system was employed, in which the RDE was the working electrode, the graphite rod was the counter electrode, and the standard hydrogen electrode was the reference electrode. The electrolyte for the HER activity test was 0.5 M H_2SO_4 (degassed with N_2). The polarization curve was obtained by linear sweep voltammetry (LSV) and corrected by iR compensation as commonly reported [26–29]. The scanning speed was 5 mV s^{-1}, and the scanning interval was − 0.1 to 0.05 V vs. RHE. The parameters of the ADT test were set as follows: scanning rate, 100 mV s^{-1}; scanning interval − 0.15 to 0.4 V vs. RHE. Electrochemical impedance spectroscopy (EIS) was performed over a frequency range of 100 kHz to 1 Hz with an AC amplitude of 5 mV. I_{ring} and I_{disk} tests were performed using an amperometric i-t curve. The Φ_{disk} and Φ_{ring} of RRDE are 0.2475 and 0.1866 cm^2 respectively. The catalyst was dropped on the disk, and constant potentials of 10 mV, 15 mV, and 25 mV were applied on the plate, respectively, for HER. The H_2 produced on the disk was collected by the platinum ring, and HOR occurred at a constant voltage of 0.7 V vs. RHE.

2.6. DFT calculation methods

DFT calculations were performed using the Vienna ab initio simulation package (VASP). The exchange–correlation interaction was described by the generalized gradient approximation (GGA) with the revised Perdew–Burke–Ernzerhof (PBE) functional. The energy cutoff was set to 550 eV. The gamma k-point mesh was set to 2 × 2 × 1. The convergence threshold in geometry optimization was set to 10^{-2} eV/Å. For self-consistent field (SCF) energy convergence, it was 10^{-6} eV. For construction of the surface models, a vacuum of 15 Å was used to eliminate interactions between periodic structures.

The $\Delta G_{Anchoring}$ was defined as $\Delta G_{Anchoring} = E_{(Slab)} - E_{(Slab\_without\_Pt)} - E_{(Pt\_atom)}$

$\Delta G_H{}^*$ was defined as $\Delta G_H{}^* = \Delta E_H{}^* + \Delta E_{ZPE} - T\Delta S_H$. $\Delta E_H{}^*$ is the hydrogen chemisorption energy expressed by the following equation: $\Delta E_H{}^* = E_{(Slab\text{-}H^*)} - E_{(Slab)} - \frac{1}{2}E_{H2}$ [30]. $E_{(Slab\text{-}H^*)}$ and $E_{(Slab)}$ are the energies of the active sites with and without H* adsorption, respectively. $E_{(Slab\_without\_Pt)}$ is the energy of the active sites before anchoring a Pt atom. ΔE_{ZPE} is the zero-point energy difference between the adsorbed and gas phases. ΔS_H is the entropy change between the adsorbed H and gas-phase H_2 at 1 atm and T is 298.15 K. The sum of them, which could be regarded as thermal correction to Gibbs free energy, could be obtained via vibrational frequency calculations. VASPKIT was used [31] to directly read the value from OUTCAR file.

3. Results and discussion

3.1. Catalyst morphology

The catalyst preparation method is illustrated in Fig. 1 and Fig. S1. Metal–organic frameworks (MOFs) are a type of organic framework composed of metal ions and organic ligands. They have a high specific surface area, many functional sites, and adjustable apertures [32,33]. We used Co_1NC carbonized by cobalt-doped ZIF-8 as the porous support (M_{Zn}:M_{Co} = 60:1 in precursor). $[PtCl_6]^{2-}/Co_1NC$ was obtained after Co_1NC adsorbed the Pt precursor (chloroplatinic acid) at room

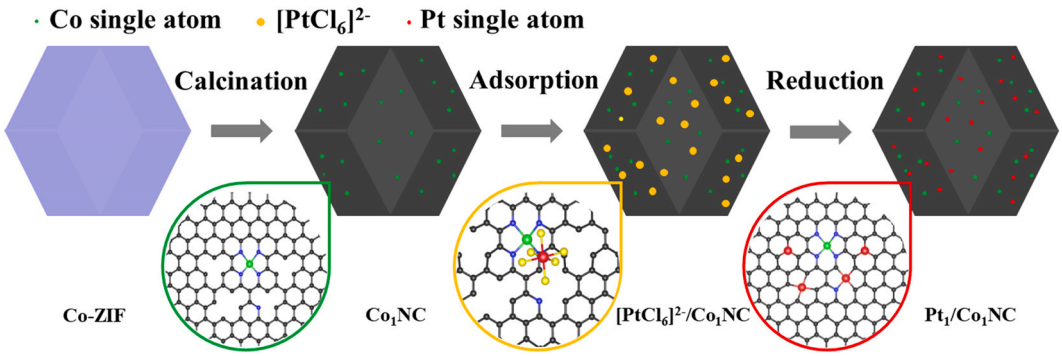

Fig. 1. Schematic illustration of the preparation of Pt_1/Co_1NC.

temperature.

The electrochemical reduction method can significantly reduce the reaction temperature and prevent particle agglomeration in simple steps as illustrated in Fig. S2 [12,34]. Therefore, we used an electrochemical reduction method to reduce Pt in $[PtCl_6]^{2-}/Co_1NC$ at room temperature to obtain Pt_1/Co_1NC. As a control sample, Pt_{NP}/NC was prepared in a manner similar to that of Pt_1/Co_1NC, but the support was obtained from pyrolyzed pure ZIF-8 powders, denoted as NC, which was prepared by the same method but contained no cobalt species (refer to the Supporting Information for more experimental and characterization details). As a result, the mass fraction of Pt was 0.5 wt% in Pt_{NP}/NC, as confirmed by inductively coupled plasma optical emission spectroscopy (ICP-OES) (the metal contents of all samples were measured in the same way), and 0.4 wt% in Pt_1/Co_1NC. Meanwhile, the mass fraction of Co was 0.17 wt% in Pt_1/Co_1NC.

However, despite the fact that the Pt loadings in Pt_1/Co_1NC and Pt_{NP}/NC were almost the same, there were significant differences between the existing forms of Pt. As shown in transmission electron microscopy (TEM) images (Fig. S3), after sintering at high temperature, Co_1NC still maintained its polyhedral morphology. So does NC in Fig. S4 with its similar morphology to Co_1NC. Moreover, no obvious particles were observed in Pt_1/Co_1NC after Pt loading (Fig. 2a and b). Meanwhile, no characteristic peaks of either metal oxides or simple substances were observed in the X-ray diffraction (XRD) spectra (Fig. S5). We also performed regular and aberration-corrected high-angle annular dark-field scanning transmission electron microscopy (HAADF-STEM) on the Pt_1/Co_1NC from a sub-atomic angle of view. It is obvious from the results (Fig. 2c and d and Fig. S6, area with good dispersibility) that bright spots, which represent transition metal species, were dispersed atomically with great abundancy at higher magnification. Furthermore, energy-dispersive X-ray (EDX) confirmed the existence of Pt and Co elements in the same area, proving that Co and Pt do not exist in the form of aggregates in Pt_1/Co_1NC (Fig. 2e and f) but are uniformly dispersed. However, from the TEM images of Pt_{NP}/NC (Fig. S7), numerous Pt particles were observed, even though the Pt content was only slightly higher (0.5 wt%). The agglomeration of Pt species occurred in the absence of Co in the precursor of the carbon support.

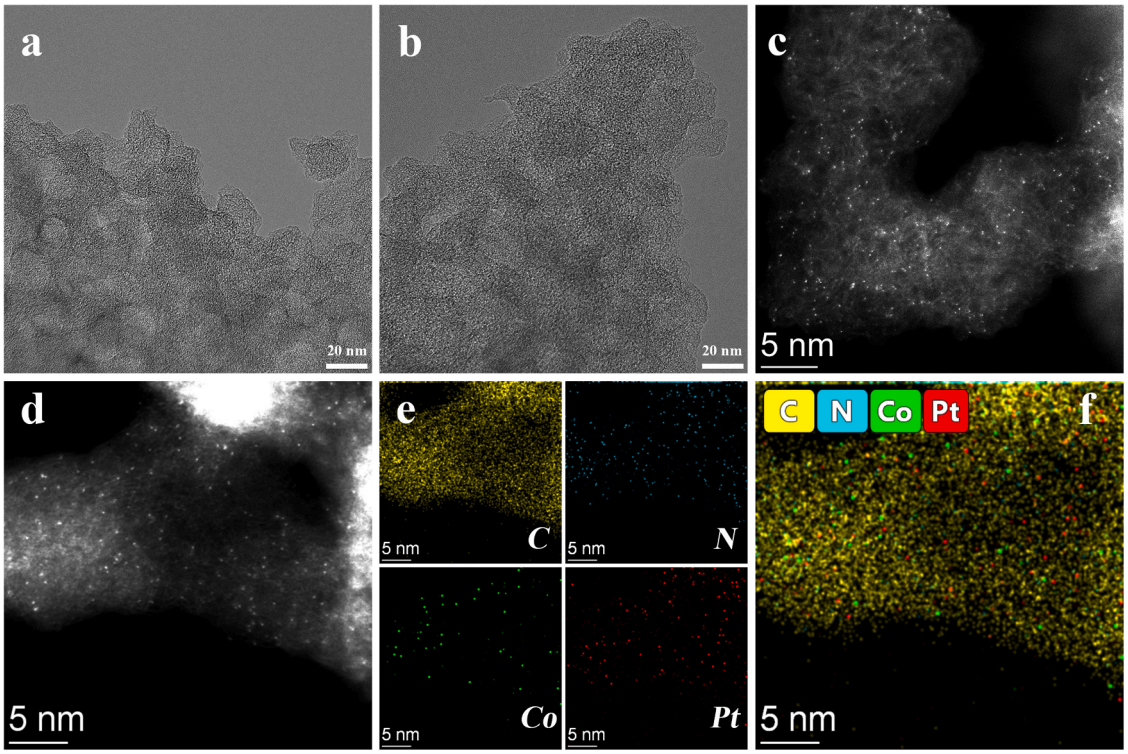

Fig. 2. (a, b) TEM images, (c, d) HAADF-STEM images, and (e, f) EDX mapping of Pt_1/Co_1NC.

3.2. Characterization

3.2.1. X-ray absorption spectroscopy

To further investigate the existing form of Pt sites, X-ray absorption near edge structure (XANES) and extended X-ray absorption fine structure (EXAFS) can be used to observe the electronic structure and coordination state of atoms. The XANES spectra of the Pt L_3-edge are shown in Fig. 3a. The area under the white line (WL) peak of the Pt L_3-edge X-ray absorption spectra can reflect the unoccupied state density of the Pt 5d orbitals [35]. Therefore, the valence states of the samples were compared based on the intensity of the WL peaks. The sequence of the valence states of Pt in the reference sample from high to low is as follows: PtO_2 > $PtCl_4$ > $PtCl_2$ > Pt_1/Co_1NC > Pt foil. With respect to the EXAFS fitting curve of Pt L_3-edge (Fig. 3b, k-space data available in Fig. S8), there is an obvious peak at 1.6 Å. This peak can be attributed to Pt-N/C, and the small peak at 2.3 Å is also associated with the Pt-N/C. A strong peak at approximately 2.6 Å in Pt foil originates from the metallic Pt—Pt bond, so its absence indicates that no Pt—Pt bond is present [36]. The coordination numbers (bond lengths) of the two Pt—C/N bonds are 3.1 (bond length is 2.05 Å) and 4.3 (bond length is 2.64 Å), respectively (Table S1). Fig. 3c shows the wavelet transform (WT) maps extracted from the EXAFS oscillations. The WT intensity maximum appears near 6.2 $Å^{-1}$ and is associated with the Pt-N/C path at ~ 1.6 Å for Pt_1/Co_1NC. Co species were also investigated by XANES and EXAFS, as shown in Fig. S9, Fig. S10 and Table S2, indicating that Co atoms were also atomically dispersed. Moreover, it should be emphasized that through the WT map showed in Fig. S9c, the X-coordinate corresponding to the peak at ~ 1.6 Å is near 5 $Å^{-1}$, which indicates that the coordinated atom of Co is a light atom, but not a heavy metal like Pt. For the same reason, the coordinated atom of Pt should also be a light atom revealed by Fig. 3c. Therefore, from the EXAFS fitting and WT results, direct interaction between Pt and Co atoms could not be detected. In summary, both Pt and Co in Pt_1/Co_1NC exist in the form of single atoms coordinated with nitrogen or carbon respectively, which is in accordance with the HAADF-STEM results.

Results from X-ray photoelectron spectroscopy (XPS) analysis further supported perspectives on the valence states of Pt atoms in Pt_1/Co_1NC and Pt_{NP}/NC obtained above. The Pt 4f XPS spectrum of Pt_1/Co_1NC is composed of two types of Pt species, Pt (II) species and Pt (IV) species (Fig. 3d). The binding energies of Pt (II) species are 73.88 eV ($4f_{7/2}$ orbitals) and 77.2 eV ($4f_{5/2}$ orbitals) [29], and the binding energies of Pt (IV) species are 74.20 eV ($4f_{7/2}$ orbitals) and 77.55 eV ($4f_{5/2}$ orbitals). However, the composition of the Pt species in Pt_{NP}/NC was different from that in Pt_1/Co_1NC. Pt_{NP}/NC contained Pt (II) species and primarily Pt (0) species (Fig. 3e). For Pt (II) species, the binding energies are 73.88 eV ($4f_{7/2}$ orbitals) and 77.2 eV ($4f_{5/2}$ orbitals), and for Pt (0) species, they are 71.53 eV ($4f_{7/2}$ orbitals) and 74.88 eV ($4f_{5/2}$ orbitals) [37]. This further validates the previous observation, obtained by TEM, that Pt in Pt_1/Co_1NC exists as a single atom, while Pt in Pt_{NP}/NC is agglomerated into particles.

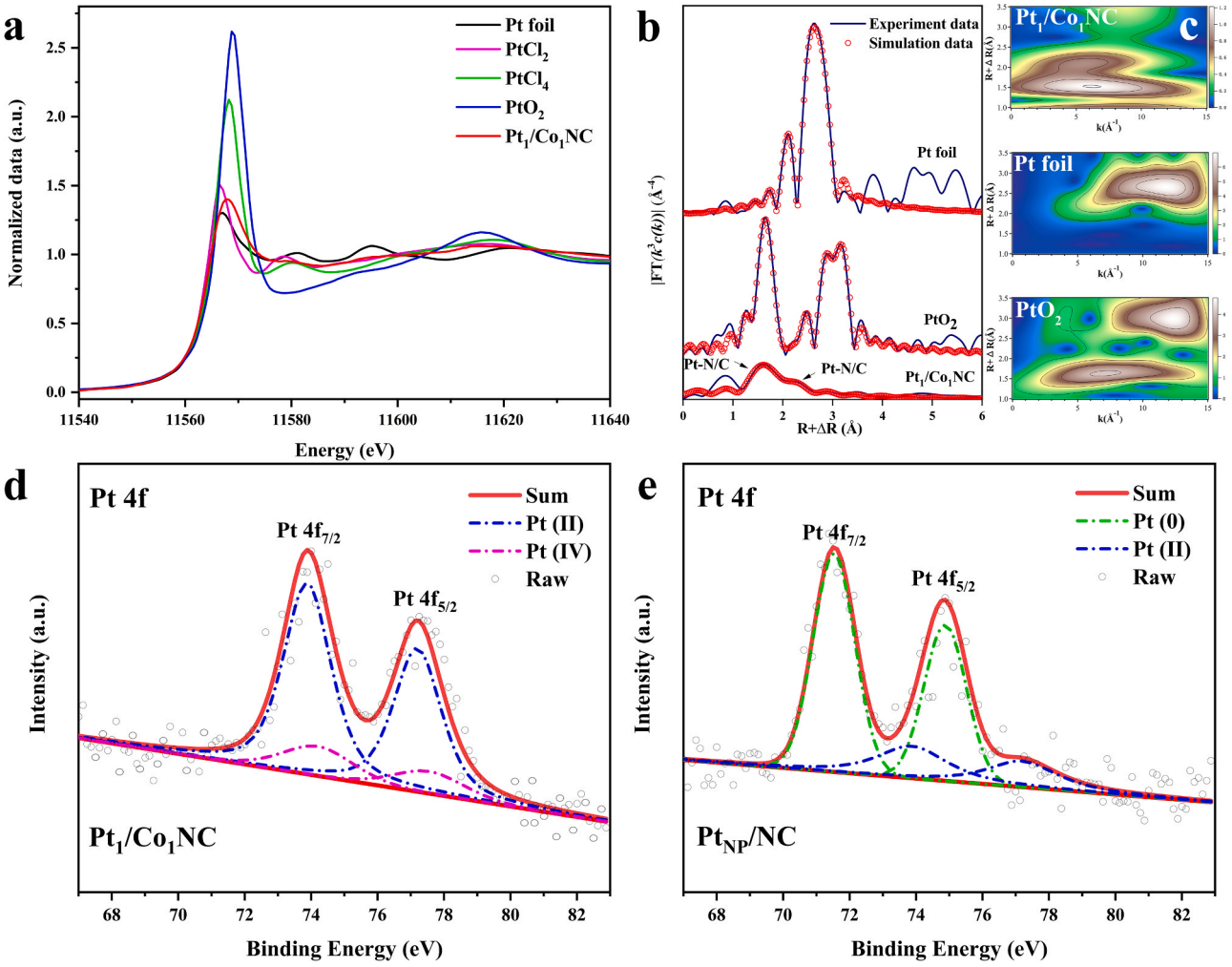

Fig. 3. (a) Pt L_3-edge XANES spectra for Pt_1/Co_1NC and reference; (b) Fourier transform Pt L_3-edge EXAFS spectra for Pt_1/Co_1NC with Pt foil and PtO_2 for reference. (c) Wavelet transform Pt L_3-edge EXAFS spectra for Pt_1/Co_1NC with Pt foil and PtO_2 for reference. High-resolution Pt 4f XPS spectra of (d) Pt_1/Co_1NC and (e) Pt_{NP}/NC.

3.2.2. Raman and XPS spectra

According to the previous characterization, adsorbed Pt precursors tend to form atomically dispersed sites in Co_1NC, while forming Pt aggregates in NC. To explore the reasons for this difference, Raman spectroscopy was used to investigate the variation before and after reduction. Raman spectra of the four samples, i.e., Co_1NC, NC, Pt_1/Co_1NC, and Pt_{NP}/NC, are shown in Fig. 4a and d. They all contain a D-band peak (~ 1350 cm^{-1}) representing disordered carbon and a G-band peak (~ 1590 cm^{-1}) representing ordered graphite [38]. However, the ratio of $Area_D/Area_G$ was quite different (Fig. 4e, the peaks have been normalized to keep a same G-band peak intensity for better visualization of the difference existed in D-band peaks). It is well known that as the ratio of $Area_D/Area_G$ increases, the corresponding carbon material is more disordered, indicating more defects [39]. The Raman spectra show that Co_1NC ($Area_D/Area_G$ = 3.48) has many more defects than NC ($Area_D/Area_G$ = 2.90). This effect brought by the Cobalt doping in the ZIF-8 precursor is also evidenced by the difference in specific surface area. For Co_1NC, it is as high as 1221.11 m^2/g, which is much higher than that of ZIF-8 without cobalt (657.55 m^2/g) (Fig. S11). This would greatly enhance the ability to maintain atomically dispersion of Pt precursor and provides strong anchoring ability as previously reported (preventing aggregation) [40]. Hence, there was also a significant difference in the defect change after loading Pt with the two supports. When Co_1NC was loaded with Pt, the ratio of $Area_D/Area_G$ decreased significantly, to 2.47. However, after loading Pt on NC, the variation was very small ($Area_D/Area_G$ = 2.69). This indicates that when Co_1NC was used as a support, more defects were exploited to anchor the Pt single atom. In contrast, when NC is used as a support, the chance of agglomeration of Pt particles increases because of scarcity defects serving as anchoring sites, and the agglomerated Pt clusters can soon grow, further reducing the probability of forming single-atom dispersed Pt sites.

The N 1s XPS spectra of the four samples also support this conclusion. As shown in Fig. 5, the N 1s XPS spectrum can be divided into peaks from different types of species: oxidized N (404.2 eV), graphitic N (401.3 eV), pyrrolic N (400.5 eV), metal N (399.1 eV), and pyridinic N (398.5 eV) [16,41]. The total nitrogen contents of Co_1NC, NC, Pt_1/Co_1NC, and Pt_{NP}/NC showed little difference, with respective values of 3.04 at%, 3.10 at%, 3.12 at%, and 3.13 at%. However, we noticed significant changes in the contents of metal N and pyridinic N. For metal N, the proportion of metal N to total nitrogen in Co_1NC was 6.25%. As NC was sintered at a high temperature of 1100 °C, the Zn species in it had almost completely evaporated, so there was no metal N in NC. After Pt loading and reduction, the proportion of metal N in total nitrogen species of Pt_1/Co_1NC increased significantly to 14.01%, and that of Pt_{NP}/NC increased slightly, to 6.50%. This is consistent with the results of the XANES and EXAFS. From Co_1NC to Pt_1/Co_1NC, the content of pyridinic N among the total nitrogen species decreases rapidly, from 21.90% to

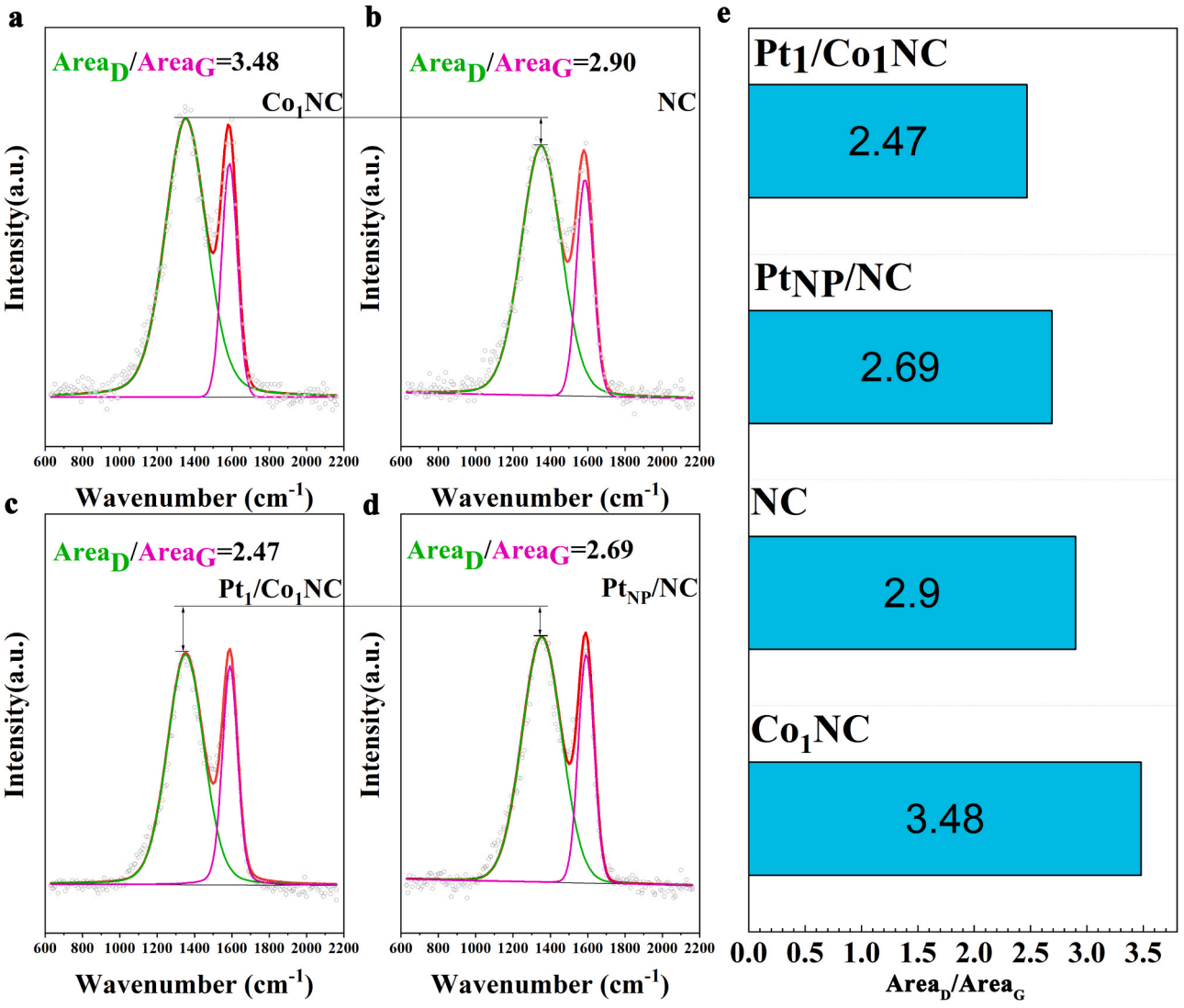

Fig. 4. Raman spectra of (a) Co_1NC, (b) NC, (c) Pt_1/Co_1NC, and (d) Pt_{NP}/NC, and (e) $Area_D/Area_G$ for the different samples.

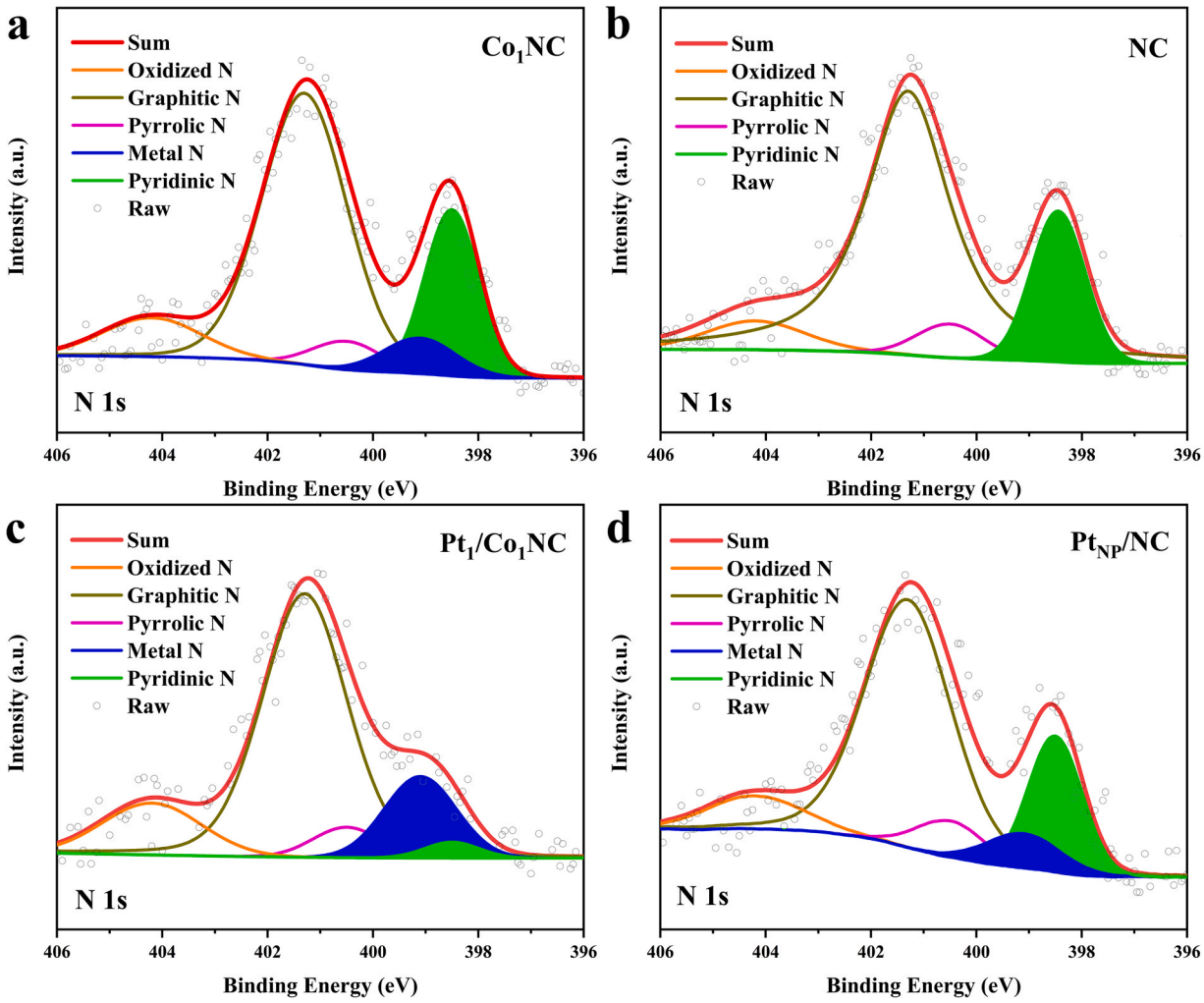

Fig. 5. XPS N 1s spectra of (a) Co_1NC, (b) NC, (c) Pt_1/Co_1NC, and (d) Pt_{NP}/NC.

2.05%, indicating that a large number of uncoordinated N-doped sites have anchored Pt atoms. However, from NC to Pt_{NP}/NC, the variation was again very small, from 20.07% to 18.98%, as most of the Pt elements formed nanoparticles (Table S3). In short, a large amount of pyridine nitrogen was converted to Pt-N when Co_1NC was used as a support for loading Pt, while only a very small amount of pyridine nitrogen was converted when using NC as support loading Pt. We can conclude that carbon defects are very beneficial to the anchoring of Pt single atoms, and pyridinic N species also play an important role in this process.

3.3. Electrochemical performance

The HER catalytic activities of Co_1NC, Pt_1/Co_1NC, Pt_{NP}/NC, and the commercial product 20 wt% Pt/C were measured using a three-electrode system in a N_2-saturated 0.5 M H_2SO_4 solution at room temperature. The linear scan voltammetry curves of the catalysts are shown in Fig. 6a. It is clear that the overpotential of Pt_1/Co_1NC is 4.15 mV to achieve a current density of 10 mA cm^{-2}, which is lower than those of Pt_{NP}/NC (22.85 mV) and commercial 20 wt% Pt/C (16.74 mV). From the point of view of mass activity, Pt_1/Co_1NC was also the best among them at an overpotential of 20 mV, with mass activity up to 32.4 A mg^{-1}_{Pt}, while Pt_{NP}/NC and 20 wt% Pt/C had values of only 2.9 A mg^{-1}_{Pt} and 0.6 A mg^{-1}_{Pt}, respectively (Fig. 6b). The turnover frequency (TOF) values of Pt_1/Co_1NC at overpotentials of 20 mV were 32.86 s^{-1}, outperforming Pt_{NP}/NC (1.3 s^{-1}@ $\eta = 20$ mv) and the majority of precious metal-based HER catalysts (Fig. 6c and Table S4) [26, 28,42–50]. The reaction kinetics were compared by comparing the Tafel slopes of the samples. The Tafel slope of Pt_1/Co_1NC (17 mV dec^{-1}) was much smaller than those of Pt_{NP}/NC (28 mV dec^{-1}) and commercial 20 wt% Pt/C (38 mV dec^{-1}) (Fig. S12), indicating a faster electron transfer process. Moreover, the much smaller semicircle in the Nyquist plots for Pt_1/Co_1NC compared with Pt_{NP}/NC reveals the promoted charge transfer behavior over the catalyst interface, which is conducive to electrocatalyst activity (Fig. S13) [17]. To further evaluate the stability of Pt_1/Co_1NC, an accelerated aging test (ADT) was performed by continuous operation of 5000 CV cycles. After the durability test, the catalytic activity of Pt_1/Co_1NC was only slightly attenuated. The overpotential became 4.69 mV to achieve a current density of 10 mA cm^{-2}, with a mass activity of 30.54 A mg^{-1}_{Pt} at an overpotential of 20 mV; after the ADT, the overpotential was increased to 24.31 mV to achieve a current density of 10 mA cm^{-2} for commercial 20 wt% Pt/C (Fig. 6d). After the stability test, the morphology of Pt_1/Co_1NC remained stable, and no agglomeration of metal particles was observed under TEM observation (Fig. S14). Moreover, the Faradaic efficiency of Pt_1/Co_1NC was also higher than that of commercial 20 wt% Pt/C (Fig. S15). Therefore, Pt_1/Co_1NC exhibits excellent HER activity and long-term performance, showing great potential for practical applications.

3.4. First principle simulation

To investigate how the atomically dispersed Pt species serve as efficient catalytic sites, a simulation based on density functional theory

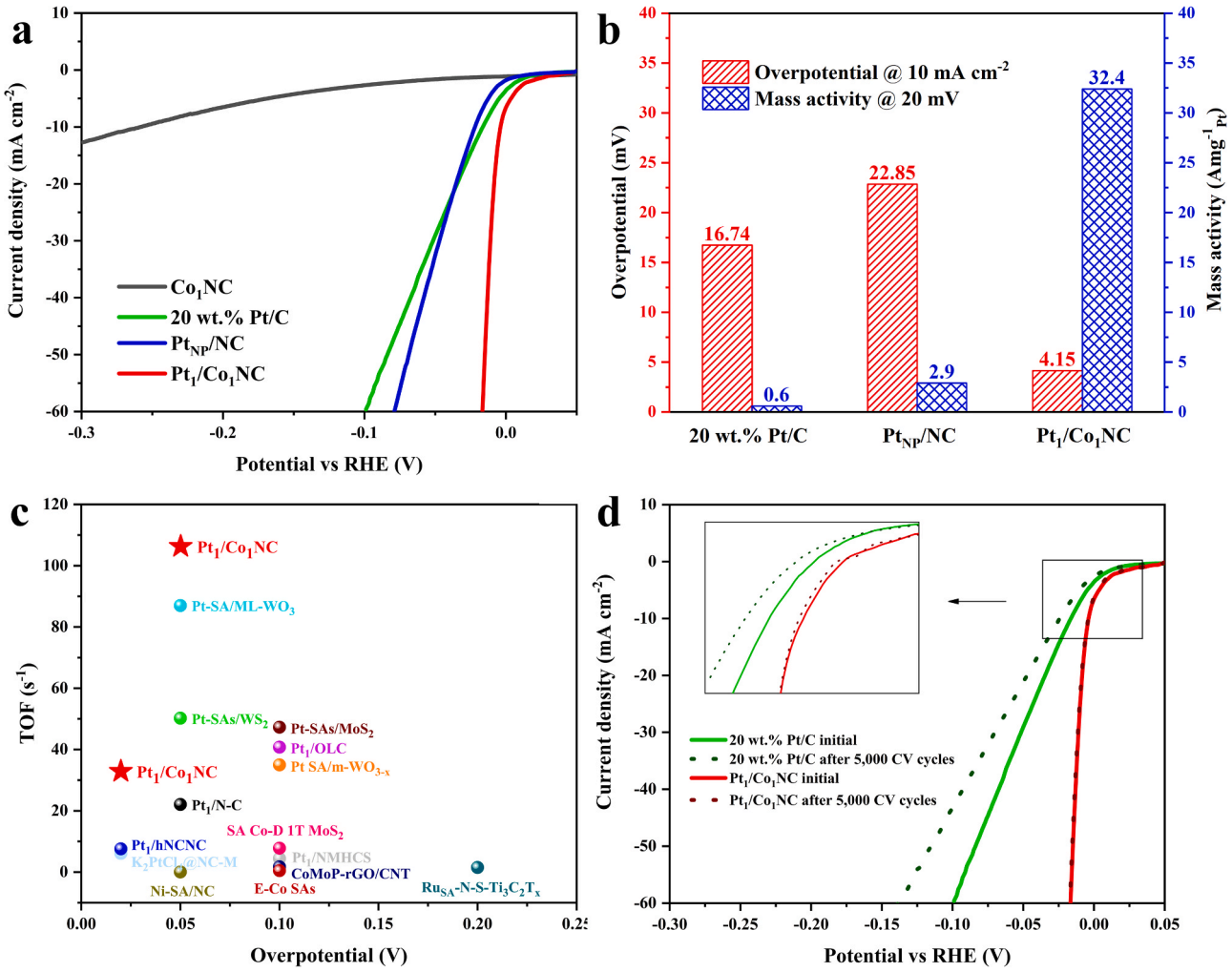

Fig. 6. (a) Polarization curves of Co_1NC, Pt_1/Co_1NC, Pt_{NP}/NC, and 20 wt% Pt/C. (b) Overpotential @ 10 mA cm^{-2} and mass activity @ 20 mV of Co_1NC, Pt_1/Co_1NC, Pt_{NP}/NC, and 20 wt% Pt/C. (c) Comparison of turnover frequency (TOF) values between Pt_1/Co_1NC and recently reported single-atom catalysts. (d) Polarization curves of Pt_1/Co_1NC and 20 wt% Pt/C before and after 5000 CV cycles.

(DFT) was conducted to obtain more insights into the HER mechanism. As previously indicated by EXAFS fitting and WT maps, no evidence for direct coordination or interaction between Pt and Co single atoms could be observed. Therefore, it might be more appropriate to regard single atoms in Pt_1/Co_1NC as isolated catalytic sites. For comparison, we constructed atomically dispersed Pt sites with different coordinating structures [27,51] and Pt crystals and examined their H adsorption Gibbs free energy (ΔG_H^*), which has been regarded as an important descriptor of HER catalytic activity [52,53]. As the $|\Delta G_H^*|$ decrease, the performance of the electrocatalyst improves. As shown in Fig. 7a and b, 12 different possible structures of Pt-N/C with three or four coordinating numbers were constructed, and their ΔG_H^* values are listed in Table S5. The $|\Delta G_H^*|$ values of Pt-C_3, Pt-C_4, and Pt-N_1C_3 were computed to be only 0.041, 0.122, and 0.264 eV, respectively, smaller than those of the Pt (111) face. Moreover, we compared the free energy changes to anchor Pt atoms between different coordinating structures (Table S6). As shown in Fig. 7c, for Pt single atoms coordinated with three carbon or nitrogen atoms, structures with more carbon atoms would be more thermodynamically favorable. $\Delta G_{Anchoring}$ (details in calculation methods) decreased from − 3.14 eV (Pt-N_3) to − 8.2 eV (Pt-C_3). Similarly, Pt-N_1C_3 and Pt-C_4 showed favoring $\Delta G_{Anchoring}$ of − 11.23 eV and − 11.49 eV compared with the coordinated structure with four other atoms. Therefore, Pt-C_3, Pt-C_4, and Pt-N_1C_3 were proven to be both favorable for thermodynamic formation and highly active as HER catalytic sites. Hence, the DFT simulation was in good agreement with previous characterization and electrochemical evaluation results. To confirm this conclusion, we further tuned the Pt loading in Pt_1Co_1NC by changing the amount of Pt precursor adsorbed. When Pt loading was reduced or increased to 0.5 and 2.5 times that of the original sample, inferior HER performance was obtained (Fig. S16). Insufficient amounts of active sites and aggregation of Pt species with excessive precursors are thought to be the respective reasons, according to the TEM characterization (Fig. S17). Through the above characterization and DFT simulation, the catalytic sites leading to high HER activity are very likely to be determined [54,55]. Combining with the previous electrochemical test results, it is suggested that the difference of catalytic sites at an atomic level has led to the final difference of catalytic performance as electrocatalyst's macro property [56]. The unique structure of atomically dispersed Pt-N/C sites formed by defect anchoring strategy has finally led to its significant improvement of HER performance compared with traditional Pt/C catalyst while greatly saving the cost.

4. Conclusion

In this study, we have proposed a mild electrochemical reduction method for defect-rich support at room temperature to prepare an excellent electrocatalyst with atomically dispersed Pt serving as an efficient HER catalytic site. Co_1NC derived from Co-doped ZIF-8 was used as a promising support with abundant pores and defects to effectively anchor Pt precursors and form atomically dispersed Pt-N/C sites.

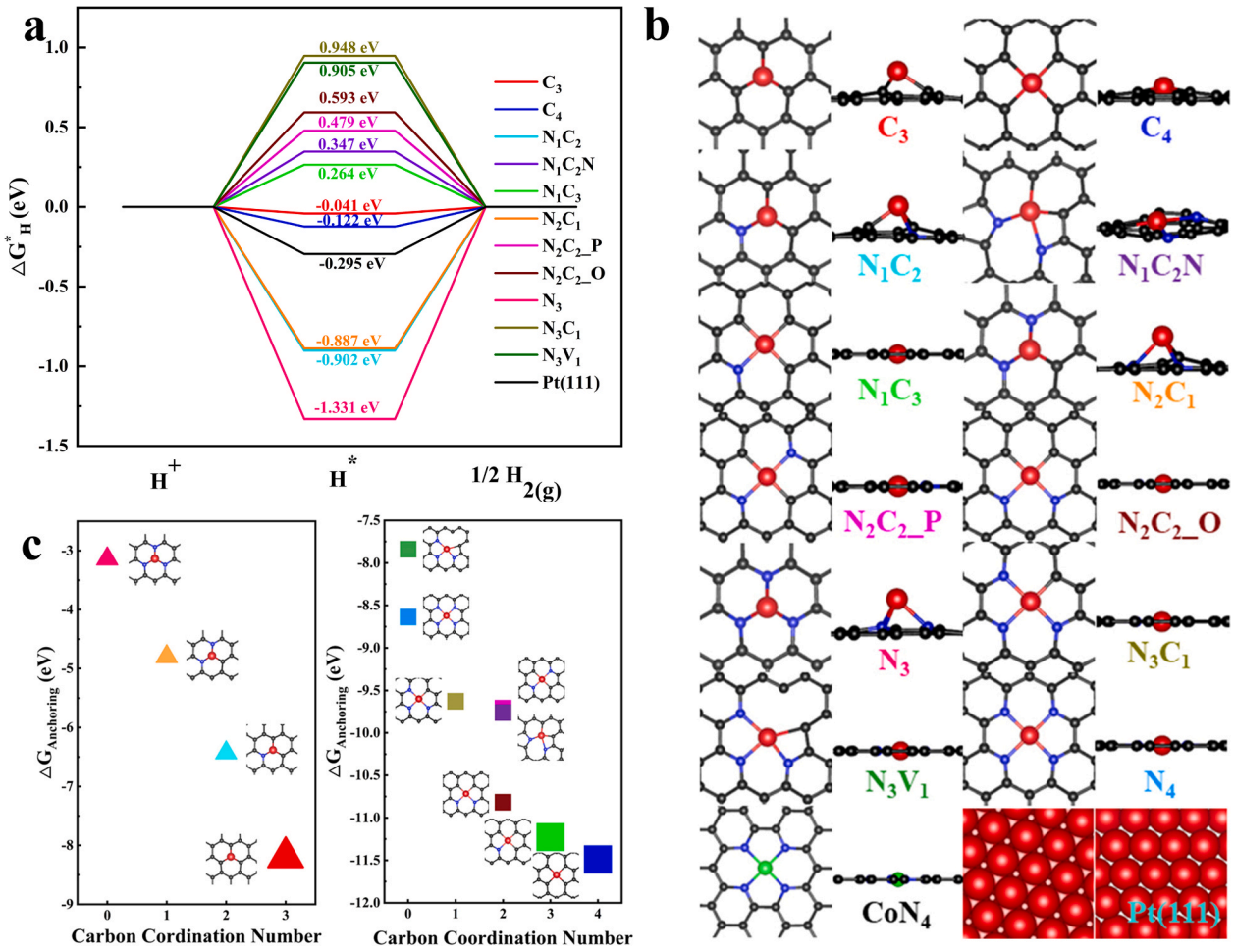

Fig. 7. (a) Calculated ΔG_H^* values of HER for various active sites. (b) Configuration of various active sites. (c) Calculated $\Delta G_{Anchoring}$ for various active sites along carbon coordination numbers.

Compared with Pt_{NP}/NC and the commercial product 20 wt% Pt/C, where Pt existed as nanoparticles, Pt_1/Co_1NC showed an overpotential as low as 4.15 mV to achieve a current density of 10 mA cm^{-2}. Its mass activity was as high as 32.4 A mg^{-1}_{Pt}, which is 54 times that of commercial 20 wt% Pt/C. Meanwhile, Pt_1/Co_1NC exhibited excellent durability. After 5000 cycles, the overpotential drop was only 0.54 mV. The results of our strategy suggest that Pt species could be firmly anchored on the defect-rich carbon support Co_1NC to form atomically dispersed Pt-N/C sites, rather than aggregates. In addition, their HER catalytic activity and precious metal utilization significantly outperformed those of a traditional electrocatalyst based on nanoparticles, which was further supported by DFT simulations. Therefore, our method could lead to marked reduction of the cost of hydrogen production with renewable electricity, which is favorable for the future hydrogen society.

Funding sources

This work was partially supported by National Key R&D Plan of China [2019YFB1504503], the National Natural Science Foundation of China [21802069], and Key R&D plan of Zhejiang Province [2020C01006].

The computation in this work was performed on High-Performance Computing Center of Collaborative Innovation Center of Advanced Microstructures, Collaborative Innovation Center of Advanced Microstructures, Nanjing University, Nanjing 210093, China.

Author contributions

Sample synthesis, experiment design and exploration were done by Yawen Chen. Rui Ding contributed to the first principle modelling. Jia Li and Jianguo Liu have given important constructive suggestions on this work in terms of idea and the article structure.

CRediT authorship contribution statement

Yawen Chen: Conceptualization, Methodology, Validation, Investigation, Writing – original draft, Visualization. **Rui Ding:** Conceptualization, Methodology, Software, Investigation, Formal analysis, Writing – original draft, Writing – review & editing. **Jia Li:** Conceptualization, Data curation, Writing – review & editing, Supervision. **Jianguo Liu:** Resources, Writing – review & editing, Supervision, Project administration.

Declaration of Competing Interest

The authors declare that they have no known competing financial interests or personal relationships that could have appeared to influence the work reported in this paper.

Appendix A. Supporting information

Supplementary data associated with this article can be found in the online version at doi:10.1016/j.apcatb.2021.120830.

References

[1] B.E. Logan, L. Shi, R. Rossi, Enabling the use of seawater for hydrogen gas production in water electrolyzers, Joule 5 (2021) 760–762.
[2] M. Li, C. Liu, B. Zhang, Using water as the hydrogen source for electrocatalytic transfer hydrogen storage, Sci. Bull. 66 (2021) 1047–1049.
[3] A. Kovač, M. Paranos, D. Marciuš, Hydrogen in energy transition: a review, Int. J. Hydrogen Energy 46 (2021) 10016–10035.
[4] J.A. Okolie, B.R. Patra, A. Mukherjee, S. Nanda, A.K. Dalai, J.A. Kozinski, Futuristic applications of hydrogen in energy, biorefining, aerospace, pharmaceuticals and metallurgy, Int. J. Hydrogen Energy 46 (2021) 8885–8905.
[5] B. Moss, O. Babacan, A. Kafizas, A. Hankin, A review of inorganic photoelectrode developments and reactor scale-up challenges for solar hydrogen production, Adv. Energy Mater. 11 (2021), 2003286.
[6] Y. Xiong, Q.T. Campbell, J. Fanghanel, C.K. Badding, H. Wang, N.E. Kirchner-Hall, M.J. Theibault, I. Timrov, J.S. Mondschein, K. Seth, R. Katz, A.M. Villarino, B. Pamuk, M.E. Penrod, M.M. Khan, T. Rivera, N.C. Smith, X. Quintana, P. Orbe, C. J. Fennie, S. Asem-Hiablie, J.L. Young, T.G. Deutsch, M. Cococcioni, V. Gopalan, H. D. Abruña, R.E. Schaak, I. Dabo, Optimizing accuracy and efficacy in data-driven materials discovery for the solar production of hydrogen, Energy Environ. Sci. 14 (2021) 2335–2348.
[7] J.N. Hansen, H. Prats, K.K. Toudahl, N. Morch Secher, K. Chan, J. Kibsgaard, I. Chorkendorff, Is there anything better than Pt for HER? ACS Energy Lett. 6 (2021) 1175–1180.
[8] C.G. Freyschlag, R.J. Madix, Precious metal magic: catalytic wizardry, Mater. Today 14 (2011) 134–142.
[9] O. Lori, L. Elbaz, Recent advances in synthesis and utilization of ultra-low loading of precious metal-based catalysts for fuel cells, ChemCatChem 12 (2020) 3434–3446.
[10] M. Luo, Y. Yang, S. Guo, Precious metal nanocrystals for renewable energy electrocatalysis: structural design and controlled synthesis, Dalton Trans. 49 (2020) 267–273.
[11] Y. Wang, D. Wang, Y. Li, Rational design of single-atom site electrocatalysts: from theoretical understandings to practical applications, Adv. Mater. 33 (2021), e2008151.
[12] Z. Zhang, C. Feng, C. Liu, M. Zuo, L. Qin, X. Yan, Y. Xing, H. Li, R. Si, S. Zhou, J. Zeng, Electrochemical deposition as a universal route for fabricating single-atom catalysts, Nat. Commun. 11 (2020) 1215.
[13] S. Ji, Y. Chen, X. Wang, Z. Zhang, D. Wang, Y. Li, Chemical synthesis of single atomic site catalysts, Chem. Rev. 120 (2020) 11900–11955.
[14] P. Yin, T. Yao, Y. Wu, L. Zheng, Y. Lin, W. Liu, H. Ju, J. Zhu, X. Hong, Z. Deng, G. Zhou, S. Wei, Y. Li, Single cobalt atoms with precise N-coordination as superior oxygen reduction reaction catalysts, Angew. Chem. Int. Ed. Engl. 55 (2016) 10800–10805.
[15] J. Yang, W.H. Li, S. Tan, K. Xu, Y. Wang, D. Wang, Y. Li, The electronic metal-support interaction directing the design of single atomic site catalysts: achieving high efficiency towards hydrogen evolution, Angew. Chem. Int. Ed. Engl. 60 (2021) 19085–19091.
[16] R. Ding, Y. Liu, Z. Rui, J. Li, J. Liu, Z. Zou, Facile grafting strategy synthesis of single-atom electrocatalyst with enhanced ORR performance, Nano Res. 13 (2020) 1519–1526.
[17] P. Kuang, Y. Wang, B. Zhu, F. Xia, C.W. Tung, J. Wu, H.M. Chen, J. Yu, Pt Single atoms supported on N-doped mesoporous hollow carbon spheres with enhanced electrocatalytic H2 -evolution activity, Adv. Mater. 33 (2021), e2008599.
[18] W. Liu, J. Ji, X. Yan, W. Liu, Y.-C. Huang, K. Wang, P. Jin, X. Yao, J. Jiang, A cascade surface immobilization strategy to access high-density and closely distanced atomic Pt sites for enhancing alkaline hydrogen evolution reaction, J. Mater. Chem. A 8 (2020) 5255–5262.
[19] W. Ni, Z. Liu, Y. Zhang, C. Ma, H. Deng, S. Zhang, S. Wang, Electroreduction of carbon dioxide driven by the intrinsic defects in the carbon plane of a single Fe-N4 site, Adv. Mater. 33 (2021), e2003238.
[20] C. Xie, D. Yan, W. Chen, Y. Zou, R. Chen, S. Zang, Y. Wang, X. Yao, S. Wang, Insight into the design of defect electrocatalysts: from electronic structure to adsorption energy, Mater. Today 31 (2019) 47–68.
[21] Q. Yang, Y. Jia, F. Wei, L. Zhuang, D. Yang, J. Liu, X. Wang, S. Lin, P. Yuan, X. Yao, Understanding the activity of Co-N4-x Cx in atomic metal catalysts for oxygen reduction catalysis, Angew. Chem. Int. Ed. Engl. 59 (2020) 6122–6127.
[22] L. Zhang, J. Fischer, Y. Jia, X. Yan, W. Xu, X. Wang, J. Chen, D. Yang, H. Liu, L. Zhuang, M. Hankel, D.J. Searles, K. Huang, S. Feng, C.L. Brown, X. Yao, Coordination of atomic Co-Pt coupling species at carbon defects as active sites for oxygen reduction reaction, J. Am. Chem. Soc. 140 (2018) 10757–10763.
[23] Y. Qu, Z. Li, W. Chen, Y. Lin, T. Yuan, Z. Yang, C. Zhao, J. Wang, C. Zhao, X. Wang, F. Zhou, Z. Zhuang, Y. Wu, Y. Li, Direct transformation of bulk copper into copper single sites via emitting and trapping of atoms, Nat. Catal. 1 (2018) 781–786.
[24] X. Yan, L. Zhuang, Z. Zhu, X. Yao, Defect engineering and characterization of active sites for efficient electrocatalysis, Nanoscale 13 (2021) 3327–3345.
[25] G. Huang, Z. Xiao, R. Chen, S. Wang, Defect engineering of cobalt-based materials for electrocatalytic water splitting, ACS Sustain. Chem. Eng. 6 (2018) 15954–15969.
[26] Z. Zhang, Y. Chen, L. Zhou, C. Chen, Z. Han, B. Zhang, Q. Wu, L. Yang, L. Du, Y. Bu, P. Wang, X. Wang, H. Yang, Z. Hu, The simplest construction of single-site catalysts by the synergism of micropore trapping and nitrogen anchoring, Nat. Commun. 10 (2019) 1657.
[27] P.Y. Kuang, Y.R. Wang, B.C. Zhu, F.J. Xia, C.W. Tung, J.S. Wu, H.M. Chen, J.G. Yu, Pt single atoms supported on n-doped mesoporous hollow carbon spheres with enhanced electrocatalytic H-2-evolution activity, Adv. Mater. 33 (2021) 9.
[28] H. Jin, S. Sultan, M. Ha, J.N. Tiwari, M.G. Kim, K.S. Kim, Simple and scalable mechanochemical synthesis of noble metal catalysts with single atoms toward highly efficient hydrogen evolution, Adv. Funct. Mater. 30 (2020), 2000531.
[29] D. Liu, X. Li, S. Chen, H. Yan, C. Wang, C. Wu, Y.A. Haleem, S. Duan, J. Lu, B. Ge, P. M. Ajayan, Y. Luo, J. Jiang, L. Song, Atomically dispersed platinum supported on curved carbon supports for efficient electrocatalytic hydrogen evolution, Nat. Energy 4 (2019) 512–518.
[30] D. Gao, X. Wu, P. Wang, H. Yu, B. Zhu, J. Fan, J. Yu, Selenium-enriched amorphous NiSe1+ nanoclusters as a highly efficient cocatalyst for photocatalytic H2 evolution, Chem. Eng. J. 408 (2021), 127230.
[31] V. Wang, N. Xu, J.-C. Liu, G. Tang, W.-T. Geng, VASPKIT: a user-friendly interface facilitating high-throughput computing and analysis using VASP code, Comput. Phys. Commun. 267 (2021), 108033.
[32] Y. Zheng, L. Zhang, H. Huang, F. Wang, L. Yin, H. Jiang, D. Wang, J. Yang, G. Zuo, ZIF-67-derived Co, Ni and S co-doped N-enriched porous carbon polyhedron as an efficient electrocatalyst for oxygen evolution reaction (OER), Int. J. Hydrogen Energy 44 (2019) 27465–27471.
[33] C.C. Hou, L. Zou, Y. Wang, Q. Xu, MOF-mediated fabrication of a porous 3D superstructure of carbon nanosheets decorated with ultrafine cobalt phosphide nanoparticles for efficient electrocatalysis and zinc-air batteries, Angew. Chem. Int. Ed. Engl. 59 (2020) 21360–21366.
[34] Y. Dong, T. Slade, M.J. Stolt, L. Li, S.N. Girard, L. Mai, S. Jin, Low-temperature molten-salt production of silicon nanowires by the electrochemical reduction of CaSiO3, Angew. Chem. Int. Ed. Engl. 56 (2017) 14453–14457.
[35] J. Zhang, Y. Zhao, X. Guo, C. Chen, C.-L. Dong, R.-S. Liu, C.-P. Han, Y. Li, Y. Gogotsi, G. Wang, Single platinum atoms immobilized on an MXene as an efficient catalyst for the hydrogen evolution reaction, Nat. Catal. 1 (2018) 985–992.
[36] R. Shen, W. Chen, Q. Peng, S. Lu, L. Zheng, X. Cao, Y. Wang, W. Zhu, J. Zhang, Z. Zhuang, C. Chen, D. Wang, Y. Li, High-concentration single atomic Pt sites on hollow CuSx for selective O2 reduction to H2O2 in acid solution, Chem 5 (2019) 2099–2110.
[37] X. Cheng, Y. Lu, L. Zheng, M. Pupucevski, H. Li, G. Chen, S. Sun, G. Wu, Engineering local coordination environment of atomically dispersed platinum catalyst via lattice distortion of support for efficient hydrogen evolution reaction, Mater. Today Energy 20 (2021), 100653.
[38] J. Li, X. Zhu, J. Wang, Z. Rui, S. Zhang, Y. Li, R. Ding, W. He, J. Liu, Z. Zou, Iron-Containing porphyrins self-assembled on ZnO nanoparticles as electrocatalytic materials for oxygen reduction, ACS Appl. Nano Mater. 3 (2020) 742–751.
[39] J. Li, M. Chen, D.A. Cullen, S. Hwang, M. Wang, B. Li, K. Liu, S. Karakalos, M. Lucero, H. Zhang, C. Lei, H. Xu, G.E. Sterbinsky, Z. Feng, D. Su, K.L. More, G. Wang, Z. Wang, G. Wu, Atomically dispersed manganese catalysts for oxygen reduction in proton-exchange membrane fuel cells, Nat. Catal. 1 (2018) 935–945.
[40] J. Liu, M. Jiao, B. Mei, Y. Tong, Y. Li, M. Ruan, P. Song, G. Sun, L. Jiang, Y. Wang, Z. Jiang, L. Gu, Z. Zhou, W. Xu, Carbon-supported divacancy-anchored platinum single-atom electrocatalysts with superhigh Pt utilization for the oxygen reduction reaction, Angew. Chem. Int. Ed. Engl. 58 (2019) 1163–1167.
[41] C. Zhao, Y. Wang, Z. Li, W. Chen, Q. Xu, D. He, D. Xi, Q. Zhang, T. Yuan, Y. Qu, J. Yang, F. Zhou, Z. Yang, X. Wang, J. Wang, J. Luo, Y. Li, H. Duan, Y. Wu, Y. Li, Solid-diffusion synthesis of single-atom catalysts directly from bulk metal for efficient CO_2 reduction, Joule 3 (2019) 584–594.
[42] W. Zang, T. Sun, T. Yang, S. Xi, M. Waqar, Z. Kou, Z. Lyu, Y.P. Feng, J. Wang, S. J. Pennycook, Efficient hydrogen evolution of oxidized Ni-N3 defective sites for alkaline freshwater and seawater electrolysis, Adv. Mater. 33 (2021), e2003846.
[43] Y. Shi, Z.R. Ma, Y.Y. Xiao, Y.C. Yin, W.M. Huang, Z.C. Huang, Y.Z. Zheng, F.Y. Mu, R. Huang, G.Y. Shi, Y.Y. Sun, X.H. Xia, W. Chen, Electronic metal-support interaction modulates single-atom platinum catalysis for hydrogen evolution reaction, Nat. Commun. 12 (2021) 6780.
[44] X. Liu, L. Zheng, C. Han, H. Zong, G. Yang, S. Lin, A. Kumar, A.R. Jadhav, N. Q. Tran, Y. Hwang, J. Lee, S. Vasimalla, Z. Chen, S.G. Kim, H. Lee, Identifying the activity origin of a cobalt single-atom catalyst for hydrogen evolution using supervised learning, Adv. Funct. Mater. 31 (2021), 2170295.
[45] H. Zhang, W. Zhou, X.F. Lu, T. Chen, X.W. Lou, Implanting isolated Ru atoms into edge-rich carbon matrix for efficient electrocatalytic hydrogen evolution, Adv. Energy Mater. 10 (2020).
[46] M. Chen, Z. Liu, X. Zhang, A. Zhong, W. Qin, W. Liu, Y. Liu, In-situ phosphatizing of cobalt-molybdenum nanosheet arrays on self-supporting rGO/CNTs film as efficient electrocatalysts for hydrogen evolution reaction, Chem. Eng. J. 422 (2021), 130355.
[47] J. Park, S. Lee, H.E. Kim, A. Cho, S. Kim, Y. Ye, J.W. Han, H. Lee, J.H. Jang, J. Lee, Investigation of the support effect in atomically dispersed Pt on WO3-x for utilization of Pt in the hydrogen evolution reaction, Angew. Chem. Int. Ed. Engl. 58 (2019) 16038–16042.
[48] Z. Zhang, J. Cai, H. Zhu, Z. Zhuang, F. Xu, J. Hao, S. Lu, H. Li, F. Duan, M. Du, Simple construction of ruthenium single atoms on electrospun nanofibers for superior alkaline hydrogen evolution: a dynamic transformation from clusters to single atoms, Chem. Eng. J. 392 (2020), 123655.
[49] S. Wang, P. Yang, X. Sun, H. Xing, J. Hu, P. Chen, Z. Cui, W. Zhu, Z. Ma, Synthesis of 3D heterostructure Co-doped Fe2P electrocatalyst for overall seawater electrolysis, Appl. Catal. B: Environ. (2021).
[50] S. Fang, X. Zhu, X. Liu, J. Gu, W. Liu, D. Wang, W. Zhang, Y. Lin, J. Lu, S. Wei, Y. Li, T. Yao, Uncovering near-free platinum single-atom dynamics during electrochemical hydrogen evolution reaction, Nat. Commun. 11 (2020) 1029.
[51] Y. Zhu, W. Sun, W. Chen, T. Cao, Y. Xiong, J. Luo, J. Dong, L. Zheng, J. Zhang, X. Wang, C. Chen, Q. Peng, D. Wang, Y. Li, Scale-up biomass pathway to cobalt

single-site catalysts anchored on N-doped porous carbon nanobelt with ultrahigh surface area, Adv. Funct. Mater. 28 (2018).
[52] T.F. Jaramillo, K.P. Jørgensen, J. Bonde, J.H. Nielsen, S. Horch, I. Chorkendorff, Identification of active edge sites for electrochemical H2 evolution from MoS2 nanocatalysts, Science 317 (2007) 100–102.
[53] X. Mao, L. Wang, Y. Xu, P. Wang, Y. Li, J. Zhao, Computational high-throughput screening of alloy nanoclusters for electrocatalytic hydrogen evolution, npj Comput. Mater. 7 (2021) 46.
[54] E. Skúlason, V. Tripkovic, M.E. Björketun, S. Gudmundsdóttir, G. Karlberg, J. Rossmeisl, T. Bligaard, H. Jónsson, J.K. Nørskov, Modeling the electrochemical hydrogen oxidation and evolution reactions on the basis of density functional theory calculations, J. Phys. Chem. C 114 (2010) 18182–18197.
[55] L. Zhang, Q. Wang, R. Si, Z. Song, X. Lin, M.N. Banis, K. Adair, J. Li, K. Doyle-Davis, R. Li, L.M. Liu, M. Gu, X. Sun, New insight of pyrrole-like nitrogen for boosting hydrogen evolution activity and stability of Pt single atoms, Small 17 (2021), e2004453.
[56] J. Yang, W. Li, D. Wang, Y. Li, Single-atom materials: small structures determine macroproperties, Small Struct. 2 (2020), 2000051.